Article

Foam with direction: unraveling the anisotropic radiation shielding properties of 2D boron nitride nanoplatelet foams

Check for updates

Kazue Orikasa[1], Cheol Park[2], Sang-Hyon Chu[2], Calista Lum [3], Tony Thomas[1], Tyler Dolmetsch[1], Luiza Benedetti[1] & Arvind Agarwal [1] ✉

Neutron radiation exposure is one of the main challenges faced during space missions. There is a critical need for advanced lightweight radiation shielding materials. Two-dimensional (2D) boron nitride nanoplatelets (BNNP) are excellent candidates for polymer matrix nanofillers due to their superior neutron shielding and thermal and mechanical properties. Furthermore, the 2D material anisotropic behavior unlocks the potential for composite property tailoring. This study fabricated ultra-lightweight lamellar BNNP foams (density 0.05 g cm^{-3} and 97.5% porous) *via* freeze-drying processing. The neutron shielding effectiveness or mass absorption coefficient of the BNNP foams with walls perpendicular to the direction of the radiation source was 14.47 cm^2 g^{-1}, while that of the foam with parallel configuration was only 8.51 cm^2 g^{-1}. The orientation-dependent neutron radiation shielding properties were modeled using the Beer-Lambert law for porous composite materials. The BNNP foam in this study has the potential to benefit advanced tailorable radiation shielding technologies for future aerospace missions.

High-energy neutron radiation exposure and extreme thermal cycling are the main challenges during space missions[1]. Neutrons are produced as secondary radiation when galactic cosmic rays (GCR) and solar energetic particles (SEP) interact with the walls of the space structure and regolith on the surface of the Moon or planets[2]. Neutrons are uncharged particles that readily pass through most materials and interact with the nuclei of the target atom[3,4]. Many sources that emit X-rays and gamma rays also tend to emit neutrons. Exposure to neutron radiation poses significant challenges for space exploration, such as human tissue damage and electronic signal disruption[5]. Polymer composites are commonly used in aerospace technology due to their low density, hydrogen richness, and ease of processing[6,7]. However, polymers have limitations such as poor thermal, mechanical, and thermal neutron shielding properties[8,9]. Hence, there is a pressing need for effective, durable radioprotective gear which is lightweight and thermally conductive in applications related to neutron radiation[10,11].

Two-dimensional (2D) boron nitride nanoplatelets (BNNP) are excellent candidates for polymer matrix fillers due to their superior thermal neutron shielding and mechanical and thermal properties[12–14]. In addition, their 2D material anisotropic behavior unlocks the potential for composite property tailoring[15,16]. In terms of thermal neutron shielding properties, the ^{10}B isotope has a thermal

neutron absorption cross-section of 3835 *barns*, which is the largest among the low Z elements[17]. BNNPs have extraordinary mechanical strength, reaching up to 950 *GPa* along their basal plane[18]. In terms of thermal properties, BNNPs have exceptionally high-temperature stability of up to 850 °C in air and thermal conductivity of up to 600 W m^{-1} K^{-1}[19].

However, the nanomaterial dispersion within polymer matrices is challenging due to their agglomeration tendency[20]. Harrison et al. produced boron nitride (BN)/polyethylene (PE) composites with randomly dispersed BNNP orientations[21]. This random dispersion limits the ability to tailor the nanocomposite properties. Subsequently, Ying et al. fabricated multilayered hexagonal BN (hBN)/PE composites *via* hot-pressing[22]. The hBN sheets were aligned throughout the composite. However, this approach is limited to a layered microstructure which constrains the composite property tailoring along different directions. The freeze-drying technique assembles 2D nanomaterials into rigid, freestanding three-dimensional (3D) architectures or foams with well-defined orientations[23]. These foams can subsequently be infiltrated with polymers to create composites of 2D materials and polymers. The freeze-drying process allows for the design of foams in terms of their pore size, morphology, and orientation by adjusting the processing parameters[24]. The foam microstructure can be designed by controlling

[1]Mechanical and Materials Engineering Department, Florida International University, Miami, FL 33174, USA. [2]Advanced Materials and Processing Branch, NASA Langley Research Center, Hampton, VA 23681, USA. [3]University of California Merced, Merced, CA 95343, USA. ✉e-mail: agarwala@fiu.edu

thermodynamic processing parameters such as mold geometry, material, and solid loading[25].

This study employed a template-free freeze-drying approach to fabricate BNNP foams with a lamellar morphology. The foam microstructure was intentionally designed to have highly aligned lamellar nanoplatelet walls to enhance the anisotropic material properties. The BNNPs were strategically arranged along the lamellar foam walls. We modeled the correlation between the freeze-drying processing variables and the resulting foam morphologies regarding wall orientation. Because of their lamellar morphology, the radiation shielding properties of the foams were investigated in various orientations. The neutron radiation shielding properties of the foams were characterized and modeled in terms of wall orientation. The Beer-Lambert law was applied as a foundation for the neutron radiation shielding properties of the BNNP foams. The effect of the porosity was considered for the BNNP foam analysis by integrating a porosity factor.

Results and discussion
BNNP foam microstructure control via freeze-drying
The freeze-drying technique was adopted to fabricate ultra-light BNNP lamellar foams with a density of $0.05 \, \text{g cm}^{-3}$ and a porosity of $97.5 \pm 0.5\%$. A total of three disk-shaped samples were produced, and their macro-scale images are presented in Supplementary Fig. 1. The lamellar morphology of the foam was designed to take advantage of the material's anisotropic properties. Each foam's microstructure consists of highly aligned interconnected nanoplatelet walls forming micro-scale pores, as shown in the top views of BNNP foam in Fig. 1a–c. It is important to note that all the foams are composed of multiple aligned lamellar domains. However, each sample has a predominant domain orientation.

The first BNNP foam presents a lamellar structure with walls parallel to the normal direction of the foam's circular face, as shown in Fig. 1a. For simplicity purposes, this foam is defined to have a *parallel orientation*. The second BNNP foam, shown in Fig. 1b, has a lamellar structure with walls oriented diagonally. This foam, in turn, is defined to have an *intermediate orientation*. The last BNNP foam shown in Fig. 1c presents a lamellar structure with walls perpendicular to the normal direction of the foam's circular face. Similarly, this foam is defined to have a *perpendicular orientation*. These three foams were produced from the same freeze-drying slurry and had the same composition and density. However, the mold size of the three foams slightly varied, as shown in Table 1.

The difference between the BNNP foam wall orientations can be explained by Newton's Law of Cooling applied to the 2D BNNP freeze-drying slurry. The rate of heat transfer Q between the freeze-drying slurry and the freezing environment is defined as:

$$Q = hA\Delta T \quad (1)$$

Here, h is the heat transfer coefficient of the system, A is the heat transfer surface area, and ΔT is the temperature gradient.

As observed in Table 1, the surface area of each mold slightly varied. A *bottom-to-side surface ratio* is introduced to quantify this mold size variation. In this work, the bottom-to-side surface ratio is defined as the ratio of the bottom circular surface area to the side surface area of the molds, as observed in Fig. 1d. The BNNP foam with parallel orientation, shown in Fig. 1a, had a bottom-to-side surface ratio of 1.17. This bottom-to-side surface ratio (close to 1.0) translates into an evenly distributed heat transfer through the bottom and side mold surfaces. The heat transferred from the bottom surface results in ice crystals growing from the bottom. These ice crystals are forced to align radially due to the heat transferred from the side mold surface, which is similar in magnitude to that of the bottom surface. As a result, the BNNP foam predominantly adopts a parallel configuration, as shown in Fig. 1e. In contrast, the BNNP foam with predominant perpendicular orientation, shown in Fig. 1c, had a bottom-to-side surface ratio of 1.52. This higher bottom-to-side surface ratio translates into a non-uniformly distributed heat transfer through the mold surfaces. The heat transfer from the mold's bottom surface dominates and creates an unbalance in the system's heat transfer rate. The heat transferred from the bottom surface drives the ice crystals to form from the bottom surface. However, since the side surface heat transfer is much lower than the bottom surface heat transfer, there is a limited force driving radial alignment. As a result, the lamellar foam adopts a perpendicular configuration, as shown in Fig. 1f.

Anisotropic thermal neutron radiation shielding properties of BNNP foam
Neutron shielding properties of the BNNP foams were analyzed with different wall orientations with respect to the probing directions. The BNNP foams were positioned such that their circular face was normal to the neutron radiation source, as shown in Supplementary Fig. 2. The decision to focus exclusively on thermal neutrons was driven by our aim to understand the influence of BNNP foam walls in various orientations. This choice is based on the fact that ^{10}B possesses the highest thermal neutron capture cross-section among low atomic number elements. However, as the neutron energy increases, the neutron capture cross-section of ^{10}B decreases. In contrast, elements such as ^1H exhibit a significantly higher fast neutron capture cross-section with increasing neutron energy.
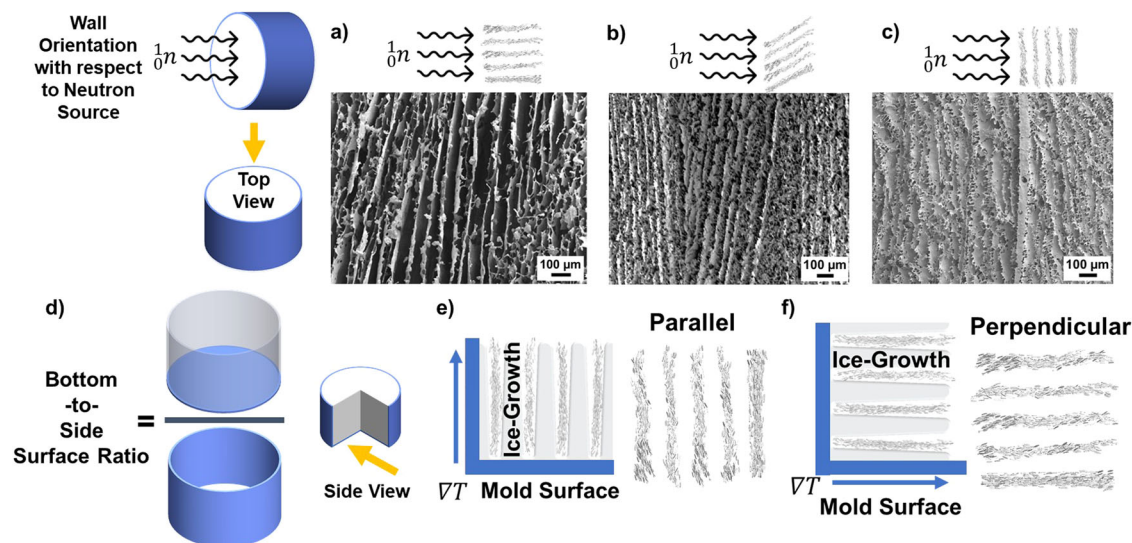
Fig. 1 | Correlation between the freeze-drying processing and the BNNP foam microstructure. Micrographs of BNNP foams with **a** parallel, **b** intermediate, and **c** perpendicular configurations. **d** Bottom-to-side surface ratio definition. Ice growth directions of BNNP foams with **e** parallel and **f** perpendicular configurations.

For analysis purposes, it was assumed that the thermal neutron energy level was of 0.5 eV. The experimental linear and mass absorption coefficients of the foams with parallel and perpendicular orientations can be observed in Table 2. The linear absorption coefficient of the foam with perpendicular configuration $\mu_\perp$ is 1.75 times that of the foam with a parallel configuration $\mu_\parallel$. The linear absorption coefficient of the foam with intermediate orientation μ_i was 0.05 mm^{-1}, in between those of the foams with parallel and perpendicular configurations. Similarly, the mass absorption coefficient of the foam with a perpendicular configuration $\mu_{m,\perp}$ is 1.70 times that of the foam with parallel orientation $\mu_{m,\parallel}$. In turn, the mass absorption coefficient of the foam with intermediate orientation $\mu_{m,i}$ was 10.39 cm^2 g^{-1}, which also lies in between values of the foams with parallel and perpendicular configurations.

In order to understand the relationship between the BNNP foam's radiation shielding properties and their microstructure, the foams with the lowest and highest mass absorption coefficients were analyzed using μ-CT scans. A 3D reconstruction videos of the foam with parallel and perpendicular walls to the neutron source can be observed in Supplementary Videos 1 and 2, respectively. The angles between the foam walls and the neutron source were quantified to establish a microstructure-property correlation. We would like to emphasize that the foams are composed of multiple domains. While these domains do not display a uniform orientation throughout, the individual domains facing the neutron source present a prevailing wall orientation.

Figure 2a, b shows the cross-section of the BNNP foam with mostly parallel and perpendicular walls with respect to the neutron source, respectively. The angles between the foam walls and neutron source were quantified and normalized by the foam diameter.

As observed in Fig. 2c, d, the angles between the average BNNP walls of the foam with parallel orientations and neutron source were 15.6 ± 17.8°. In contrast, the angles between the foam with perpendicular walls and neutron source were 76.9 ± 19.1°, as observed in Fig. 2e, f.

The ability to model the neutron radiation shielding properties of 2D BNNP foams as a function of their morphology is fundamental for their property design. The mass absorption coefficient μ_m of a homogeneous and continuous material can be approximated via the Beer-Lambert Law[26,27]:

$$\mu_m = \frac{\mu}{\rho} = \frac{1}{\rho X} \ln\left(\frac{I_0}{I}\right) \tag{2}$$

Here, μ is the BNNP foam linear absorption coefficient, ρ is the BNNP foam density, X is the BNNP foam thickness, I_0 is the number of transmitted neutron fluxes without the shielding BNNP foam, and I is the number of transmitted neutron fluxes with the BNNP composite.

The linear absorption coefficient of a continuous and homogeneous bulk composite material $\mu_{l,b}$ is defined as the following:

$$\mu_{l,b} = \sum_{n=1}^{n} \mu_{an} N_n \tag{3}$$
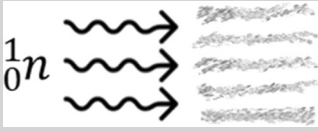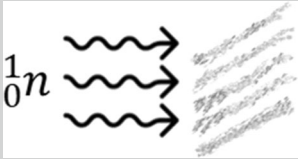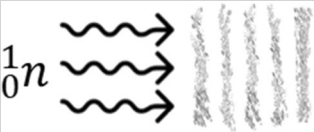
Here, n is the nth element in the composite, μ_{an} is the atomic cross-section of the nth element and N_n is the number of atoms per unit volume of the nth element. The atomic cross-section of the atoms depends on the radioactive source energy. The elemental composition of the BNNP foams was measured via energy dispersive X-ray spectroscopy (EDS), which confirms the composition of the BNNP foam can be observed in Supplementary Fig. 3. This model only approximates the BNNP foam bulk material linear absorption coefficient and does not consider the effect of porosity. The Am/Be source used during the tests produced fast neutrons with a 4.5 MeV energy. The neutron energy was lowered by placing a 25 mm thick plain polyethylene (PE) block between the neutron source and the samples, resulting in a dose equivalent rate of 320 mrem h^{-1}, as shown in Fig. 3.

As can be observed, the atomic cross-section of each element drastically depends on neutron energy[28]. The neutron absorption cross-section of each BNNP foam element as a function of the neutron energy is listed in Table 3. The BNNP foams are composed of hBN as the 2D material, styrene-butadiene rubber (SBR) as the binding agent, and sodium carboxymethyl cellulose (CMC-Na) as the dispersing agent. ^{10}B has an exceptionally high atomic cross-section of 3835 barns when the neutron source energy is

Table 1 | BNNP foam wall orientations with respect to freeze drying mold bottom and side surface areas

|	Parallel	Intermediate	Perpendicular
Bottom surface area (mm^2)	502.7	514.7	514.7
Side surface area (mm^2)	429.2	402.1	337.8
Bottom-to-side surface ratio	1.17	1.28	1.52

Table 2 | Experimental and computed linear and mass absorption coefficients of BNNP foams with parallel, intermediate, and perpendicular configurations

	Parallel	Intermediate	Perpendicular
Linear absorption coefficient experimental (mm^{-1})	$\mu_\parallel = 0.04$	$\mu_i = 0.05$	$\mu_\perp = 0.07$
Mass absorption coefficient experimental ($cm^2 g^{-1}$)	$\mu_{m,\parallel} = 8.51$	$\mu_{m,i} = 10.39$	$\mu_{m,\perp} = 14.47$
Linear absorption coefficient (thermal neutron energy) computed (mm^{-1})	$\mu_{\parallel,thermal} = 0.062$		$\mu_{\perp,thermal} = 0.085$
Mass absorption coefficient (thermal neutron energy) computed ($cm^2 g^{-1}$)	$\mu_{m,\parallel,thermal} = 12.4$		$\mu_{m,\perp,thermal} = 17.0$
Linear absorption coefficient (fast neutron energy) computed (mm^{-1})	$\mu_{\parallel,fast} = 0.00015$		$\mu_{\perp,fast} = 0.0002$
Mass absorption coefficient (fast neutron energy) computed ($cm^2 g^{-1}$)	$\mu_{m,\parallel,fast} = 0.03$		$\mu_{m,\perp,fast} = 0.04$
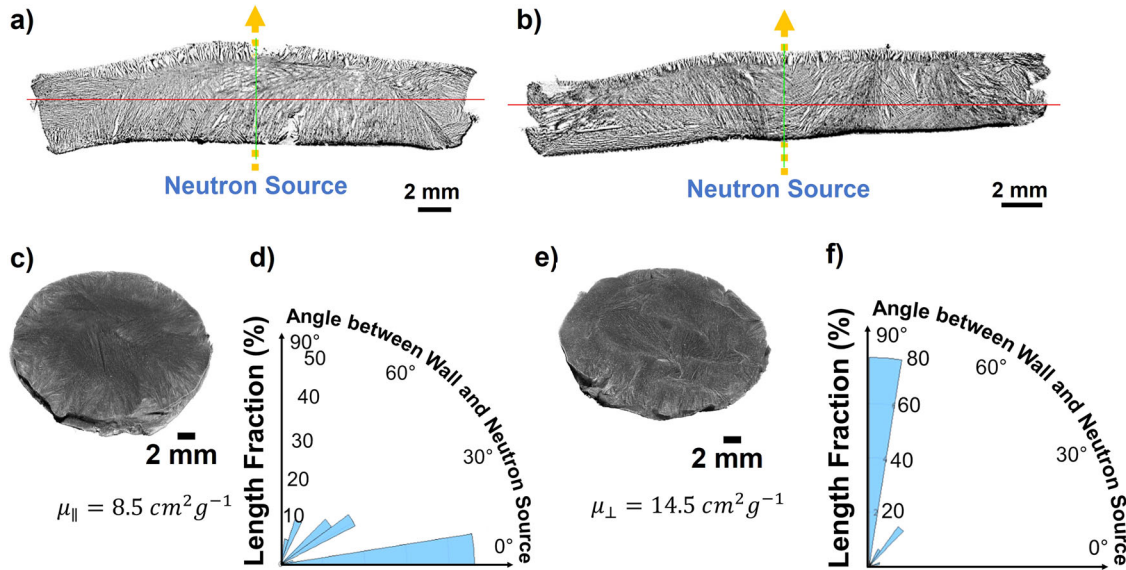
Fig. 2 | BNNP foam wall orientation with respect to the neutron source. BNNP foam cross-sections with lamellar walls **a** parallel and **b** perpendicular to the neutron source. **c** Top view of foam with parallel orientation. **d** Angle between the walls and the neutron source of the foam with parallel configuration. **e** Top view of the foam with perpendicular orientation. **f** Angle between the walls and the neutron source of the foam with perpendicular configuration.
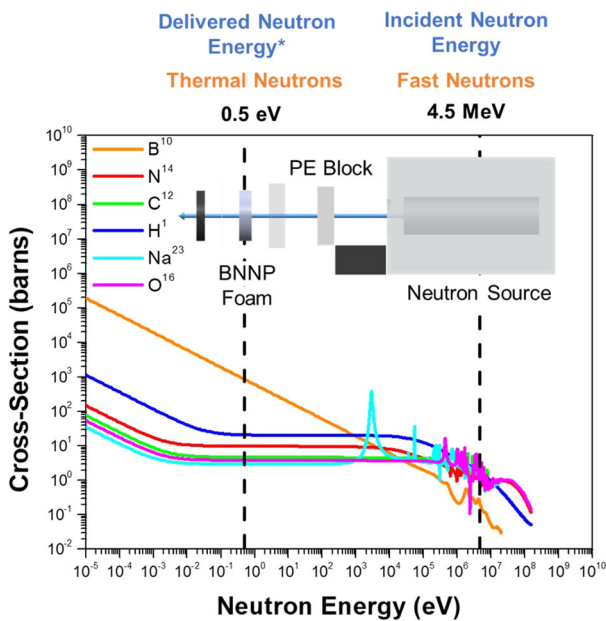
*For analysis purposes, it is assumed that the delivered neutron energy level is 0.5 eV.

Fig. 3 | Atomic cross-section of each BNNP foam element as a function of neutron energy.

<0.5 eV. As a result, ^{10}B is the most dominant BNNP foam element for thermal neutron absorption. However, as the neutron source energy increases to 4.5 MeV, the atomic cross-section of ^{10}B atoms severely decreases to 0.2439 barns. In contrast, the atomic cross-section of H^1 decreases from 21.01 barns at 0.5 eV to 1.739 barns at 4.5 MeV. H^1 becomes the dominant element for neutron absorption at higher neutron energies, with the highest atomic cross-section among all the BNNP foam elements. The linear and mass absorption coefficients were experimentally measured under mostly thermal neutron exposure. However, the computed linear and mass absorption coefficients were calculated assuming both thermal (0.5 eV) and fast neutron (4.5 MeV) exposure. The analysis was carried out

assuming both levels of energy to obtain insight into the neutron shielding behavior of the BNNP foams as a function of energy level.

The linear absorption coefficient of the BNNP foam bulk material was calculated under thermal and fast neutron energies using the linear absorption coefficient of a bulk composite material Eq. (3). The linear absorption coefficient of the BNNP foam bulk composite material under thermal neutron energy was calculated to be 0.25 mm^{-1}. In contrast, the linear absorption coefficient of the BNNP foam bulk composite material under fast neutron energy was 0.0007 mm^{-1}.

To accurately approximate the linear absorption coefficient of the BNNP foams, the effect of porosity must be considered. The porosity effect in the linear absorption coefficient of BNNP foams μ can be described by the following[29]:

$$\mu = \phi\mu_{air} + (1 - \phi)\mu_{l,b} \tag{4}$$

Here, ϕ is the apparent foam porosity, μ_{air} is the linear absorption coefficient of air $(4.77 \times 10^{-10}\,\mathrm{cm}^{-1})$, and $\mu_{l,b}$ is the linear absorption

Table 3 | Atomic cross-section of each BNNP foam element as a function of neutron energies

Chemical formula	Element	Atomic cross-section (*barns*)	
		Thermal neutron energy (<0.5 eV)*	**Fast Neutron Energy (4.5 MeV)**
BN (BNNP) 2D Material	B^{10}	3835	0.2439
	N^{14}	9.931	1.263
C$_{20}$H$_{22}$ (SBR) Binding Agent	C^{12}	4.750	1.668
	H^1	21.01	1.739
C$_8$H$_{15}$NaO$_8$ (CMC-Na) Dispersing Agent	C^{12}	4.750	1.668
	H^1	21.01	1.739
	Na^{23}	2.994	1.226
	O^{16}	3.861	1.313

*For analysis purposes, it is assumed that the delivered neutron energy level is 0.5 eV.
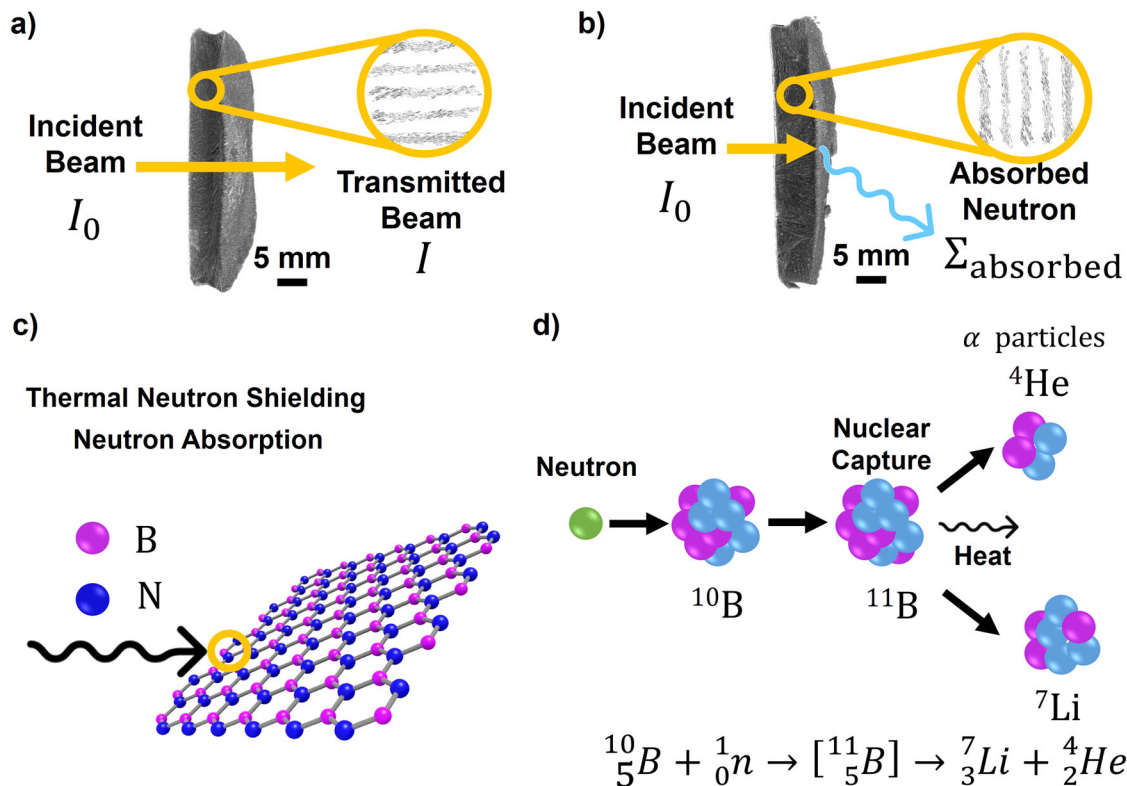
Fig. 4 | Correlation between the foam microstructure and the neutron shielding behavior of the BNNP foams. Interaction between the neutron source and BNNP foams with **a** parallel and **b** perpendicular orientation, respectively. **c** Neutron interaction with BNNP atomic structure, and **d** neutron capture mechanism of ^{10}B atoms.

coefficient of the BNNP foam bulk material. The BNNP foam apparent porosities ϕ, which are the 2D porosities of the foam face exposed to the neutron source, were calculated *via* image processing of the μ-CT scans. The BNNP foam with walls parallel to the neutron source had an apparent porosity of $\phi_\parallel = 0.75$, while the foam with perpendicular configuration had an apparent porosity of $\phi_\parallel = 0.66$.

The apparent porosity measurement is a 2D projection that represents the fraction of void spaces within the material, and it directly affects the path that neutrons take through the material[27,30,31]. After incorporating these apparent porosity values into Eq. (4), theoretical linear absorption coefficients of BNNP foams under thermal and fast neutron energy exposures were obtained for the foams with parallel $\mu_\parallel$ and perpendicular $\mu_\perp$ wall orientations. These computed linear and mass absorption coefficients of the BNNP foams with parallel and perpendicular orientations are listed in Table 2.

The computed $\mu_{\parallel,\text{thermal}}$ value was 1.55 times that of the experimental $\mu_\parallel$ value. Similarly, the computed $\mu_{\perp,\text{thermal}}$ value was 1.21 times that of the experimental $\mu_\perp$ value. In terms of the mass absorption coefficients, the computed $\mu_{\text{m},\parallel,\text{thermal}}$ value was 1.46 times that of the experimental $\mu_{\text{m},\parallel}$ value. In contrast, the computed $\mu_{\perp,\text{thermal}}$ value was 1.17 times that of the experimental $\mu_\perp$ value. The differences between the computed (thermal neutron energy) and experimental linear and mass absorption coefficient values can be attributed to not all the neutrons interacting with the foam being thermal neutrons. The atomic cross-section of the atoms depends on the radioactive source energy, as shown in Fig. 3. Our analysis considers thermal neutron atomic cross-sections exclusively. As illustrated in Fig. 3, the energy of the fast neutrons produced by the Am/Be source is lowered by a PE block to produce mostly thermal neutrons. However, it is possible that interactions between the BNNP foams and neutrons with higher energy than that of thermal neutrons could have led to the observed experimental linear and mass absorption coefficients that were lower than the computed values.

Under fast neutron energy, the computed $\mu_{\parallel,\text{fast}}$ value was 0.37 times that of the experimental $\mu_\parallel$ value. Similarly, the computed $\mu_{\perp,\text{fast}}$ value was 0.28 times that of the experimental $\mu_\perp$ value. In terms of the mass absorption coefficients, the computed $\mu_{\text{m},\parallel,\text{fast}}$ value was 0.35 times that of the experimental $\mu_{\text{m},\parallel}$ value. In contrast, the computed $\mu_{\perp,\text{fast}}$ value was 0.47 times that of the experimental $\mu_\perp$ value. This significant difference between the computed (fast neutron energy) and experimental linear and absorption coefficient values can be attributed to the fact that most neutrons interacting with the BNNP foams were thermal neutrons. As a result, the fast neutron atomic cross-section of the BNNP foam elements does not accurately represent the neutron shielding behavior of the BNNP foam. Thus, thermal neutron atomic cross-sections are suitable for approximating the linear absorption coefficient of the BNNP foams in both parallel and perpendicular configurations. We would like to note that there are many unknown variables that can influence the radiation shielding test results, such as slight neutron source-sample misalignment and variation in sample dimensions. Nevertheless, the difference between the experimental and computational values appears rather minor, and the observed trend remains consistent.

While this analysis can estimate the mass absorption coefficients of the foam based on apparent porosity, it is crucial to recognize that radiation can penetrate the foam on a much smaller scale, akin to a permeation test. This aspect may not be fully captured by porosity measurements obtained from μ-CT scan images and should be considered.

Furthermore, provided that the thickness of the shielding foam does not surpass the threshold of full shielding saturation, this analysis remains applicable for approximating the mass absorption coefficient. Foams exhibiting superior ^{10}B dispersion tend to exhibit enhanced shielding effectiveness up to a certain thickness, as neutron channeling is more prone to occur in composites with poorly dispersed boron, such as in the case of foams with a parallel orientation.

The parallel foam configuration is such that multiple air-filled pores face the radiation source, as depicted in Fig. 4a. Thus, the parallel foam
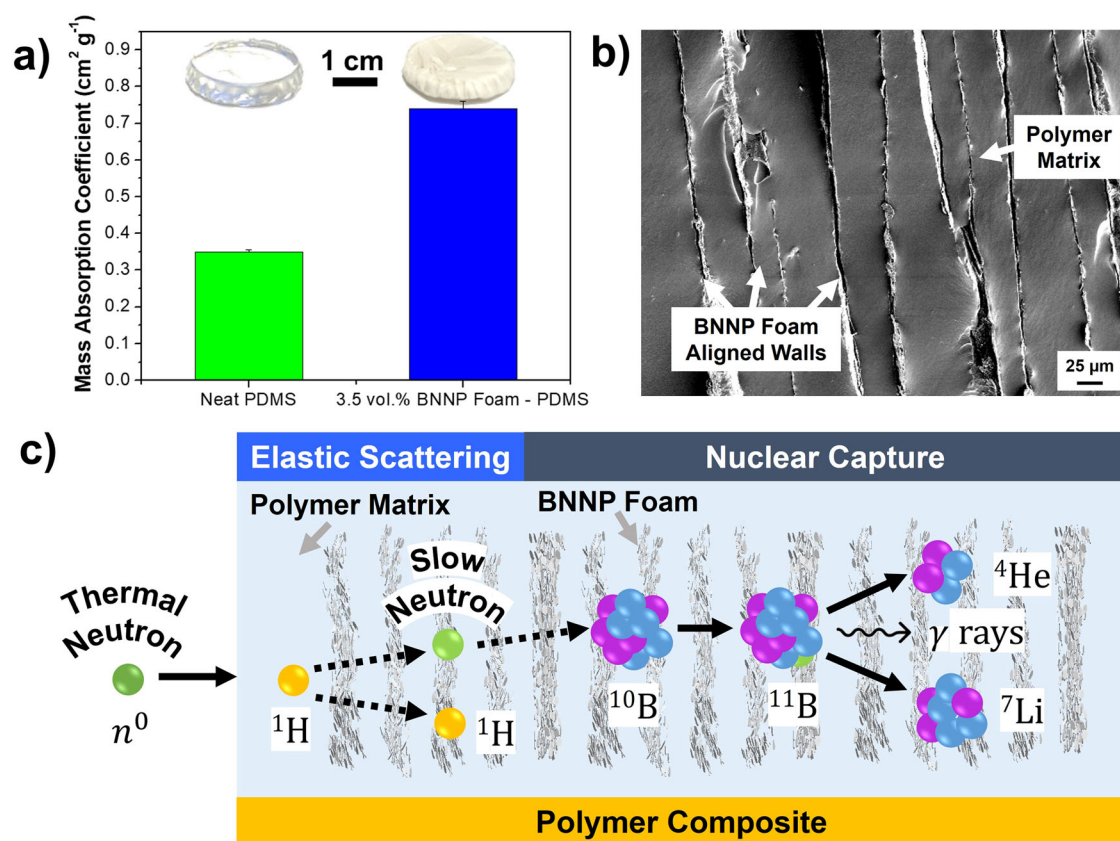
Fig. 5 | Neutron radiation shielding properties of BNNP foam-PDMS. a Mass absorption coefficient of neat PDMS and BNNP foam-PDMS, **b** BNNP foam-PDMS microstructure, and **c** thermal neutron shielding mechanisms of BNNP foam-PDMS.

orientation allows more thermal neutrons to pass through as fewer [10]B atoms are available for neutron absorption. In contrast, the higher thermal neutron radiation shielding of foams with perpendicular configuration can be attributed to the increased exposure of the BN nanoplatelet basal plane to thermal neutrons compared to foams with parallel walls, as shown in Fig. 4b. This basal-plane exposure increases the number of [10]B atoms exposed for nuclear capture, as seen in Fig. 4c. In the perpendicular configuration, the BN particles are uniformly distributed throughout the thickness, resembling a well-dispersed pattern. In contrast, in the parallel configuration, the boron particles exhibit poor dispersion, forming large aggregates along the thickness.
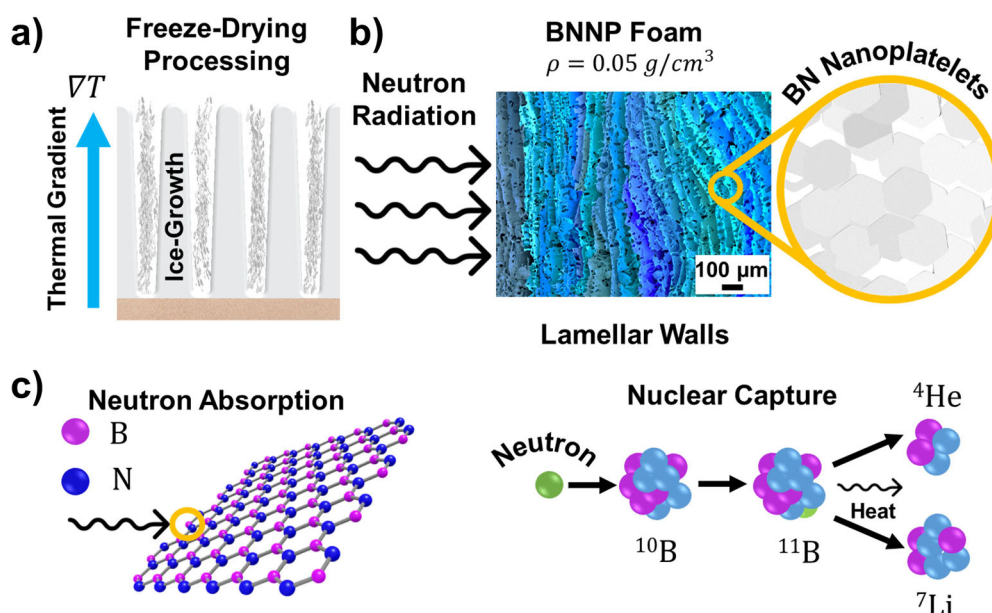
The thermal neutron shielding mechanism of BNNPs consists of the nuclear capture of slow neutrons by [10]B atoms. The thermal neutrons are captured by [10]B as a single nuclear capture event that is represented as the following reaction[32]:

$$^{10}B + n \rightarrow {}^{4}He\,(1.47\,MeV) + {}^{7}Li\,(0.84\,MeV) + \gamma\,(0.84\,MeV) \qquad (5)$$
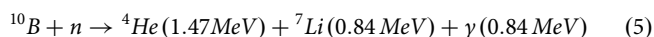
Otherwise, these thermal neutrons are likely to be scattered by ^{1}H, which is present in the binding (SBR) and dispersing (CMC-Na) agents, until they collide with [10]B atoms[33]. The absorption of these thermal neutrons leads to the nucleus's excitation, followed by the emission of α particles, gamma radiation, and Li[7], as observed in Fig. 4d. The neutron radiation test results revealed excellent radiation shielding properties with a highly orientation-dependent shielding behavior. Liquid polymers, which are hydrogen-rich materials, can subsequently infiltrate these ultralight BNNP foams to form a dense nanocomposite with enhanced neutron shielding properties. This strategy was designed to address a wide spectrum of neutron radiation scenarios, including those thermal and fast neutrons. As a proof-of-concept, the BNNP foams were infiltrated with

polydimethylsiloxane (PDMS), as observed in Fig. 5. The addition of only 3.5 vol.% of BNNP foam into PDMS doubled its mass absorption coefficient, as shown in Fig. 5a. The lamellar structure of the BNNP foam is retained when infiltrated by PDMS, as shown in Fig. 5b. The BNNP foam-PDMS neutron shielding mechanisms involve elastic scattering and nuclear capture. As per the principle of energy conservation, isotopes with a similar mass of neutrons, such as hydrogen, can induce the most significant energy loss during elastic scattering. PDMS facilitates effective neutron scattering by leveraging its abundant hydrogen content. Subsequently, slow neutrons are captured by [10]B, which is characterized by its exceptionally large thermal neutron absorption cross-section of 3835 barns. The thermal neutron shielding mechanism of the BNNP foam-PDMS can be observed in Fig. 5c. However, we would like to emphasize that the primary focus of the present study remains to investigate the thermal neutron shielding capabilities of BNNP foams.

We have developed an ultra-lightweight BNNP foam with a density of 0.05 g cm⁻³ and a porosity of 97.5 ± 0.5%. The lamellar microstructure of the BNNP foam endows it with anisotropic neutron radiation shielding properties. The excellent radiation shielding capabilities of BNNP foam make it a suitable candidate for developing lightweight materials with excellent thermal management properties for space applications. The neutron radiation shielding properties of the BNNP foam were analyzed using the Beer-Lambert law for porous composite materials. The correlation between the BNNP foam freeze-drying fabrication, microstructure, and resulting anisotropic radiation shielding properties can be observed in Fig. 6. The findings suggest that the BNNP foam developed in this study has the potential to advance tailorable radiation shielding technologies for future aerospace missions, addressing the critical need for effective neutron radiation protection in space exploration and other aerospace applications.

Fig. 6 | Correlation between the freeze-drying processing, microstructure, and neutron shielding properties of BNNP foam. a Freeze-drying processing. **b** Neutron radiation shielding behavior of BNNP foams. **c** Neutron capture mechanism of ^{10}B atoms.

Methods

BNNP particle characterization

The hexagonal boron nitride (hBN) nanoplatelets, described as boron nitride nanoplatelets (BNNP), were obtained from pH Matter Inc. (Columbus, OH, USA). The BNNP particles have a flake-like morphology with a particle size varying from 100 nm to 3 μm along their basal direction and a thickness ranging from 40 to 65 nm. The microstructure of the BNNP particles was characterized *via* Scanning Electron Microscopy (SEM JEOL JSM-F100, JEOL Ltd. Tokyo, Japan). Before characterization, the particles were dispersed *via* tip sonication (Vibra-Cell VCX750, Sonics & Materials, Inc., Newtown, CT, USA) using a tip diameter of 19 mm and amplitude of 40% for 30 min.

Freeze-drying processing of BNNP foams

A total of three highly dispersed and lightweight BNNP foams (density 0.05 g cm^{-3} and 97.5 ± 0.5% porosity) were fabricated *via* freeze-drying processing. Deionized water was used as the freezing agent. Styrene-butadiene rubber (SBR, MTI Corporation, Richmond, CA, USA) was used as a binding agent to hold the BNNPs together after sublimation. Sodium carboxymethyl cellulose (CMC-Na, Mw ~700,000, Millipore Sigma, Burlington, MA, USA) was used as a dispersing agent. The freeze-drying slurry is composed of 93 wt.% deionized water, 4 wt.% BNNPs, and 2 wt.% SBR, and 1 wt.% CMC-Na. First, CMC-Na and SBR were vortex mixed in deionized water for 30 min at room temperature. Then, the BNNPs were added to the solution and vortex mixed for 60 min at room temperature. The BNNP solution was then bath sonicated (42 kHz) for 15 min at room temperature to obtain well-dispersed BNNP slurry. The freeze-drying slurry was poured into three cylindrical copper (Cu) foil molds. The molds varied in terms of their surface areas, which are discussed in the results and analysis section. The slurry was subjected to a freezing process for 4 h at –56 °C and ambient pressure. Then, the frozen slurry was subjected to a sublimation process for 24 h at –56 °C and pressure of 1 Pa in a freeze drier (Pro-Freeze Dryer PLT300, ProLab Inc., Fort Worth, TX, USA). The resulting products were rigid freestanding porous networks of BNNPs.

Microstructure characterization

Field emission scanning electron microscopy (FE-SEM JEOL JSM-F100, JEOL Ltd. Tokyo, Japan) was used to analyze the BNNP foam micro-structure and energy dispersive X-ray spectroscopy (EDS). The foams samples were coated with gold via vacuum sputtering prior to imaging and

EDS analysis. An electron-accelerating voltage of 3 kV was applied for imaging and 10 kV for EDS analysis. The elemental composition of the foams obtained *via* EDS can be observed in Supplementary Fig. 3.

Micro-computed tomography (μ-CT) scans (SkyScan 1272 CMOS) were obtained to acquire a 3D reconstruction of the BNNP foams. A 4-μm voxel size with a source voltage of 50 kV and source current of 200 μA was used. An exposure time of 750 ms with a rotation step of 0.1° was used. The μ-CT scans were analyzed *via* ImageJ, an image processing program, to calculate BNNP foam wall orientation with respect to the radiation source and the foam apparent porosity values. The angles between the foam walls and neutron source were quantified from the cross-section view of the scans. These angles were calculated for each foam domain. Subsequently, the length of each domain was normalized by the entire foam diameter to obtain the length fraction. The data was represented through a graph of length fraction *vs* angle between the foam walls and the neutron source.

Neutron radiation shielding characterization

The radiation shielding tests were conducted at the National Aeronautics and Space Administration (NASA) Langley Research Center through the LaRC Radiation Test Facility. Supplementary Fig. 2 demonstrates the neutron radiation shielding testing setup.

The neutron source was an Americium/Beryllium (Am/Be) radioactive source of 1 *Curie*, which produces fast neutrons (4.5 *MeV*). The detection foil was a 1.25" Indium foil (0.5 *mm*, 19 *barns*). A polyethylene (PE) block was placed between the fast neutron source (4.5 *MeV*) to moderate the neutron energy and produce mostly thermal neutrons. The dose equivalent rate of the exposed sample was 320 mrem h^{-1}. The dose equivalent rate measurement was carried out using a Ludlum Portable (Model 2363) Survey Neutron survey meter. The dose equivalent rate was measured via a Prescila proton recoil scintillator probe (Model 42-41 L) employing a detection range of 0.1 mrem h^{-1} to 1 rem h^{-1}. The foam was held using a plastic sample box and was covered with parafilm to maintain the BNNP foam integrity. It was ensured that the sample holders did not affect the radiation shielding measurements. The foams were exposed to the thermal neutron source for a total of 6 h.

Data availability

The authors declare that the data supporting the findings are available within the paper and its supplementary information. The corresponding authors can provide data upon reasonable request.

References

1. Park, J., Kim, M., Choi, S. & Sun, J.-Y. Self-healable soft shield for γ-ray radiation based on polyacrylamide hydrogel composites. *Sci. Rep.* **10**, 21689 (2020).
2. Zhang, S. et al. First measurements of the radiation dose on the lunar surface. *Sci. Adv.* **6**, eaaz1334 (2020).
3. Thibeault, S. A. et al. Nanomaterials for radiation shielding. *MRS Bull.* **40**, 836–841 (2015).
4. Hirst, C. A. et al. Revealing hidden defects through stored energy measurements of radiation damage. *Sci. Adv.* **8**, eabn2733 (2022).
5. Thibeault, S. A. et al. Radiation shielding materials containing hydrogen, boron, and nitrogen: Systematic computational and experimental study - Phase I., No. HQ-E-DAA-TN33851 (2012).
6. Yost, D. C., Friedman, A. L., Hanbicki, A. T. & Grossman, J. C. 2D monolayers for superior transparent electromagnetic interference shielding. *ACS Nano* **16**, 9498–9509 (2022).
7. Camargo, P. H. C., Satyanarayana, K. G. & Wypych, F. Nanocomposites: synthesis, structure, properties and new application opportunities. *Mater. Res.* **12**, 1–39 (2009).
8. Odegard, G. Constitutive modeling of nanotube–reinforced polymer composites. *Compos. Sci. Technol.* **63**, 1671–1687 (2003).
9. Balazs, A. C., Emrick, T. & Russell, T. P. Nanoparticle polymer composites: Where two small worlds meet. *Science* **314**, 1107–1110 (2006).
10. Kang, J. H. et al. Multifunctional electroactive nanocomposites based on piezoelectric boron nitride nanotubes. *ACS Nano* **9**, 11942–11950 (2015).
11. El-Khatib, A. M. et al. Gamma attenuation coefficients of nano cadmium oxide/high density polyethylene composites. *Sci. Rep.* **9**, 16012 (2019).
12. Lei, W. et al. Boron nitride colloidal solutions, ultralight aerogels and freestanding membranes through one-step exfoliation and functionalization. *Nat. Commun.* **6**, 8849 (2015).
13. Han, J., Du, G., Gao, W. & Bai, H. An anisotropically high thermal conductive boron nitride/epoxy composite based on nacre-mimetic 3D Network. *Adv. Funct. Mater.* **29**, 1900412 (2019).
14. Rasul, M. G., Kiziltas, A., Arfaei, B. & Shahbazian-Yassar, R. 2D boron nitride nanosheets for polymer composite materials. *Npj 2D Mater. Appl.* **5**, 56 (2021).
15. Song, H. et al. Two-dimensional materials for thermal management applications. *Joule* **2**, 442–463 (2018).
16. Glavin, N. R. et al. Emerging applications of elemental 2D materials. *Adv. Mater.* **32**, 1904302 (2020).
17. Chen, X., Dmuchowski, C. M., Park, C., Fay, C. C. & Ke, C. Quantitative characterization of structural and mechanical properties of boron nitride nanotubes in high temperature environments. *Sci. Rep.* **7**, 11388 (2017).
18. Hyun, W. J. et al. High-modulus hexagonal boron nitride nanoplatelet gel electrolytes for solid-state rechargeable lithium-ion batteries. *ACS Nano* **13**, 9664–9672 (2019).
19. Guerra, V., Wan, C. & McNally, T. Thermal conductivity of 2D nano-structured boron nitride (BN) and its composites with polymers. *Prog. Mater. Sci.* **100**, 170–186 (2019).
20. Idowu, A., Boesl, B. & Agarwal, A. 3D graphene foam-reinforced polymer composites—A review. *Carbon* **135**, 52–71 (2018).
21. Harrison, C. et al. Polyethylene/boron nitride composites for space radiation shielding. *J. Appl. Polym. Sci.* **109**, 2529–2538 (2008).
22. Shang, Y. et al. Multilayer polyethylene/ hexagonal boron nitride composites showing high neutron shielding efficiency and thermal conductivity. *Compos. Commun.* **19**, 147–153 (2020).
23. Thomas, T. et al. Engineering graphene-ceramic 3D composite foams by freeze drying. *Adv. Eng. Mater.* **23**, 2001546 (2021).
24. Niksiar, P. et al. External field assisted freeze casting. *Ceramics* **2**, 208–234 (2019).
25. Thomas, T. & Agarwal, A. A facile and scalable approach in the fabrication of tailored 3D graphene foam via freeze drying. *Materials* **14**, 864 (2021).
26. Nurazila, M. Z., Hafizal, Y. & Megat Harun, M. A. Neutron attenuation and mechanical properties of polymer composites filled with boron carbide particles. *IOP Conf. Ser. Mater. Sci. Eng.* **785**, 012005 (2020).
27. Liu, B., Gu, Y., Liu, Y., Wang, S. & Li, M. Space neutron radiation shielding property of continuous fiber and functional filler reinforced polymer composite using Monte Carlo simulation. *Compos. Part Appl. Sci. Manuf.* **168**, 107483 (2023).
28. National Nuclear Data Center: Brookhaven National Laboratory. Experimental Nuclear Reaction Data (EXFOR) Database.
29. Oraby, M. Methodology and algorithm to correct the thermal neutron porosity for the effect of rare elements and rock minerals with high neutron absorption probability. *J. Pet. Explor. Prod. Technol.* **12**, 547–554 (2022).
30. Dong, C. et al. Thermally insulating $GdBO_3$ ceramics with neutron shielding performance. *Int. J. Appl. Ceram. Technol.* **19**, 1428–1438 (2022).
31. Yorov, K. E. et al. $[B_{10}H_{10}]^{2-}$ nanoclusters covalently immobilized to hybrid SiO_2 aerogels for slow neutron shielding applications. *ACS Appl. Nano Mater.* **5**, 11529–11538 (2022).
32. Cheraghi, E., Chen, S. & Yeow, J. T. W. Boron nitride-based nanomaterials for radiation shielding: A review. *IEEE Nanotechnol. Mag.* **15**, 8–17 (2021).
33. Ramirez-Cuesta, A. J., Jones, M. O. & David, W. I. F. Neutron scattering and hydrogen storage. *Mater. Today* **12**, 54–61 (2009).

Author contributions

K.O. fabricated the foams, conducted microstructural and neutron radiation shielding characterization, and performed theoretical calculations. L.B. contributed to the foam microstructural characterization via μ-CT scanning. C.P. and S.C. contributed to the neutron radiation shielding characterization of the foams. T.D. contributed to the fabrication-microstructure analysis of the foams. T.T. contributed to the project idea design. A.A. conceived the project idea, led, and oversaw the project, and finalized the manuscript.

Competing interests

The authors declare no competing interests.

Ethics

The authors affirm that the current study adheres to inclusion and ethics criteria.

Additional information

Supplementary information The online version contains supplementary material available at
https://doi.org/10.1038/s41699-024-00451-2.

Correspondence and requests for materials should be addressed to Arvind Agarwal.

Reprints and permissions information is available at
http://www.nature.com/reprints

Publisher's note Springer Nature remains neutral with regard to jurisdictional claims in published maps and institutional affiliations.

Foam with Direction: Unraveling the Anisotropic Radiation Shielding Properties of 2D Boron Nitride Nanoplatelet Foams

Kazue Orikasa[1], Cheol Park[2], Sang-Hyon Chu[2], Calista Lum[3], Tony Thomas[1], Tyler Dolmetsch[1], Luiza Benedetti[1], Arvind Agarwal[1]*

[1]Mechanical and Materials Engineering Department

Florida International University, Miami, FL, 33174, USA

[2]Advanced Materials and Processing Branch, NASA Langley Research Center, Hampton, VA 23681, USA
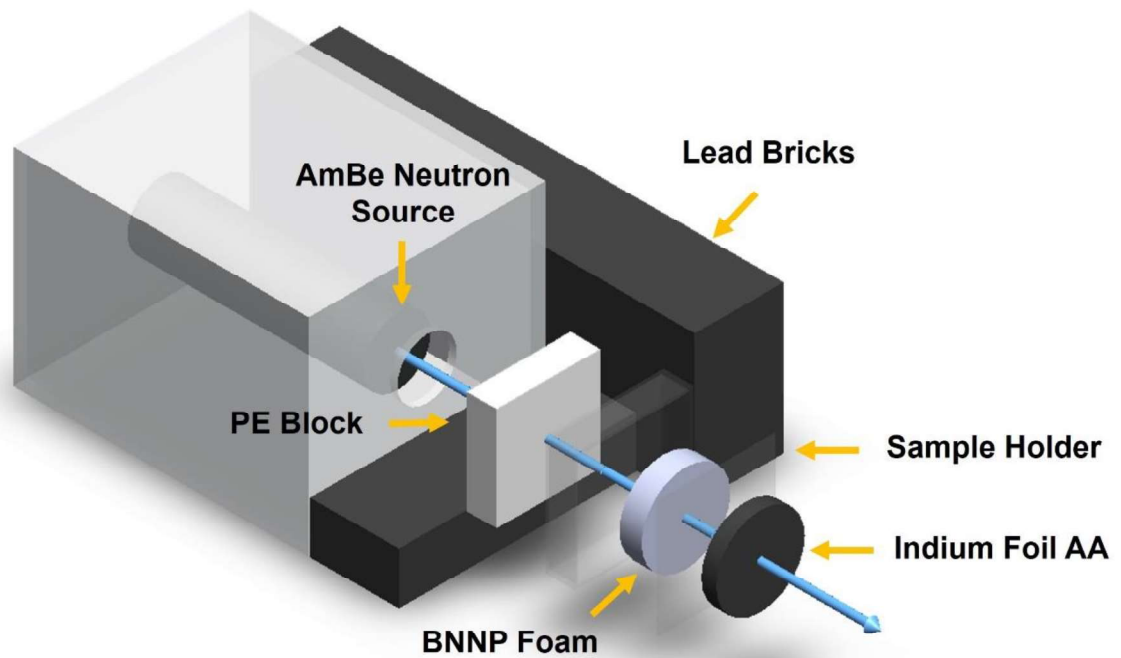
[3]University of California Merced, Merced, CA 95343, USA

*Corresponding Author: Arvind Agarwal, Ph.D., agarwala@fiu.edu
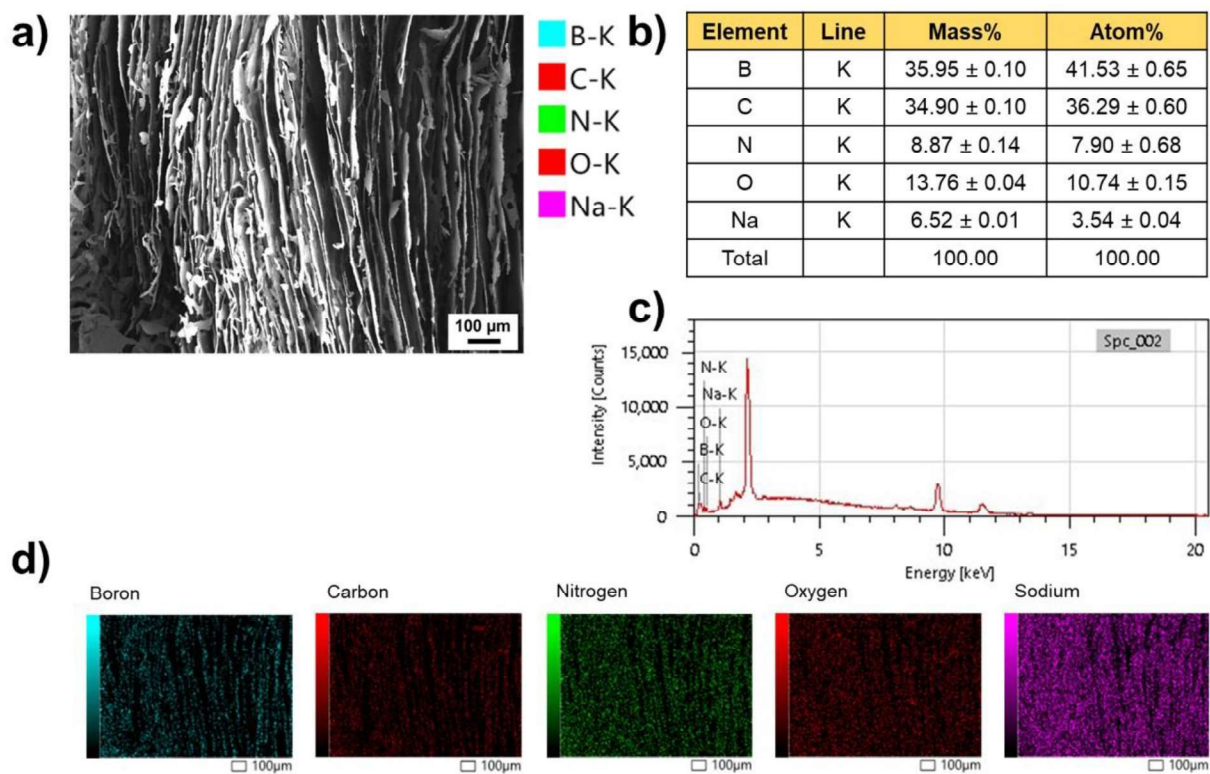
Supplementary Figures

Supplementary Figure 1. BNNP foam macrographs: BNNP foam with a) parallel, b) intermediate, and c) perpendicular walls to the neutron source

Supplementary Figure 2. Neutron radiation shielding test setup at LaRC Radiation Test Facility

Element	Line	Mass%	Atom%
B	K	35.95 ± 0.10	41.53 ± 0.65
C	K	34.90 ± 0.10	36.29 ± 0.60
N	K	8.87 ± 0.14	7.90 ± 0.68
O	K	13.76 ± 0.04	10.74 ± 0.15
Na	K	6.52 ± 0.01	3.54 ± 0.04
Total		100.00	100.00

Supplementary Figure 3. Elemental composition of BNNP foam: a) microstructure, b) elemental mass and atomic % distribution, c) EDS spectra, and d) elemental mapping